Self-organized carbon-rich stripe formation from competitive carbon and aluminium segregation at Fe 0.85 Al 0.15 (1 1 0) surfaces

Zongbei Dai, Patrizia Borghetti, Younes Mouchaal, Stephane Chenot, Pascal David, Jacques Jupille, Gregory Cabailh, Rémi Lazzari

Self-organized carbon-rich stripe formation from competitive carbon and aluminium segregation at $Fe_{0.85}Al_{0.15}(110)$ surfaces

Zongbei Dai[1], Patrizia Borghetti[1], Younes Mouchaal[1], Stéphane Chenot[1], Pascal David[1], Jacques Jupille[1], Gregory Cabailh[1], Rémi Lazzari[1,*]

[a] *CNRS, Sorbonne Universités, Institut des NanoSciences de Paris, UMR 7588, 4 Place Jussieu, F-75005 Paris, France*

Abstract

By combining Scanning Tunnelling Microscopy, Low Energy Electron Diffraction and X-ray Photoelectron Spectroscopy, it was found that the surface of A_2 random alloy $Fe_{0.85}Al_{0.15}(110)$ is significantly influenced by the segregation of aluminium but also of carbon bulk impurities. Below $\sim$ 900 K, carbon segregates in the form of self-organized protruding stripes separated by $\sim$ 5 nm that run along the $[001]_B$ bulk direction and cover up to 34 % of the surface. Their C 1s spectroscopic signature that is dominated by graphitic carbon peaks around 900 K. Above this temperature, the surface carbon concentration decays by redissolution in the bulk, whereas an intense aluminium segregation is observed giving rise to a hexagonal superstructure. The present findings is interpreted by a competitive segregation between the two elements.

Keywords: iron aluminide, segregation, random alloy, carbon

1. Introduction

In response to the environmental imperative of reduction of CO_2 emissions from cars, steel industry develops new generations of highly alloyed light steel grades by using high concentrations of alloying elements such as aluminium [1]. In parallel, iron aluminide is a promising candidate for high

*Corresponding author

Email address: remi.lazzari@insp.jussieu.fr (Rémi Lazzari)

temperature structural materials because of its high melting point, excellent formability and good resistance to oxidation [2]. However, during steel processing, complex phenomena of segregation due to alloying elements occur at surfaces or grain boundaries. These latter impact material properties [3, 4] such as corrosion resistance and mechanical behaviour; above all, wettability during galvanization becomes a major concern that refers to questions related to metal-oxide interfaces [5, 6, 7, 8]. Either as an alloying element or as an impurity, carbon is commonly present on iron and steel surfaces since the range of bulk solubility of carbon in iron is low ($\lesssim$ 200 ppm) [9]; the precipitation of carbides (Fe_3C ϵ-cementite or Fe_5C_2 κ-Hägg carbides) in the bulk embrittles steel. Even if a clear tendency towards carbon segregation is predicted by *ab initio* calculations on Fe(100) and Fe(110) [10, 11], there exists during annealing of body-centred Fe single crystal surfaces a complex interplay [12] between the formation of bulk carbide, surface carbidic species, graphite and graphene [13] either upon segregation of bulk impurities [14, 15, 16], dissociation of carbon species [17, 18, 13] or diffusion of carbon deposited on purpose [19]. On Fe(100) [14, 15, 16], in the range of solubility of carbon in iron, the nature of segregated carbon depends on the bulk temperature. Below a dissolution temperature, carbon forms graphite islands while above, a $c(2 \times 2)$ superstructure appears at saturation; the segregation equilibrium can be described by a Langmuir-Mac Lean equation [12] with a segregation enthalpy of -85 kJ.mol^{-1}. In near-field microscopy, carbon on Fe(100) appears in the form of lines of nanometer lateral scale arranged in a zig-zag configuration along $[110]_B$ and $[1\bar{1}0]_B$ directions [20]; the self-organization is mediated through interactions between carbon segregated at hollow sites at a coverage of 2/3 with a $c(3\sqrt{2} \times 2)$ superstructure. On Fe(110), carbon is predicted to occupy the long-bridge site [10] although electron diffraction experiments are not so conclusive [21]. However upon exceeding the limit of solubility, a metastable phase of cementite Fe_3C precipitates in the bulk while usually surface graphite forms. But when a third element comes into play, the landscape becomes much more complex. A co-alloying element can induce on carbon segregation synergetic or competive effects [22, 21]. For instance, carbon suffers from site competition from sulfur or silicon on Fe(100) [15, 23], a competition governed by diffusivities and segregation enthalphies. Moreover, segregation of carbon in alloys may lead to the stabilization of metastable bulk compounds or even surface compounds that do not have any bulk counterpart such as in the case of FeCrC alloys [12, 24].

Regarding iron aluminide which is the topic of this work, at low carbon contents, the body-centred α phase exists in a disordered random alloy phase (Strukturbericht symbol A_2) in the low aluminium concentration corner of the bulk phase diagram [25, 26, 27]; at higher aluminium content ($\gtrsim$ 25 %-at.), this disordered α phase transforms into ordered states of type B_2 and $D0_3$. The noticeable solubility for carbon in the A_2 solid phase, that goes up to 1.5% at., has been observed to largely shift the temperatures of the phase transitions between all the polymorphs A_2, B_2, $D0_3$ [26]. But at higher carbon content, a face-centred cubic solid solution (γ phase) and a ternary intermetallic (κ carbide phase) of defective perovskite structure [27] ($E2_1$ in the stoichiometric form Fe_3AlC) can be stabilized as well as graphite. If surfaces of iron alumines were shown to be prone to aluminium enrichment for disordered A_2 as well as for ordered B_2 alloys [28, 29, 30, 31, 32, 33, 34, 35], the effect of a third element such as carbon was poorly explored up to now. On FeAl(110), density functional calculations predict that adsorption of carbon on FeAl(110) is highly exothermic but endothermic with respect to graphite [11]. Blum *et al.* demonstrated that the co-segregation of (C, Al, S) at the surface of $Fe_{0.97}Al_{0.03}(100)$ does not take place; the sequence of segregation with temperature C $\rightarrow$ Al $\rightarrow$ S follows the measured segregation enthalpies. While C and S form a full monolayer, Al gives rise only to a $c(2 \times 2)$ reconstruction at this surface [23].

It has been chosen herein to study the segregation at the dense $Fe_{0.85}Al_{0.15}(110)$ surface between 300 and 1100 K as a model system for aluminium alloyed-steel since, in that temperature range, the alloy matrix corresponds to the ferritic A_2 solid solution as in the case of the industrial grades. The effect of an unknown carbon bulk content in the crystal leads to a puzzling segregation behaviour in the form of C-rich stripes. This paper is organized as follows. After a presentation of the methods used (Sect. 2), the spectroscopic fingerprints and the nature of carbon segregation will be discussed (Sect. 3.1). Carbon segregation upon annealing in the form of self-organized stripes will be evidenced as well as aluminium surface enrichment by near-field imaging (Sect. 3.2) and electron diffraction (Sect. 3.2.2).

2. Experimental methods

Experiments have been performed in a ultra-high vacuum set-up composed of a preparation (base pressure $3.\,10^{-10}$ mbar) and a characterization

(base pressure $< 1.10^{-10}$ mbar) chamber. The disk-shaped single crystal substrate of $Fe_{0.85}Al_{0.15}$ (diameter 6 mm, thickness 2 mm) purchased from Mateck GmbH [36] was cut within 0.1° from the $[110]_B$ orientation and polished down to the lowest achievable roughness. According to the bulk Fe-Al phase diagram [25], the 15 % atomic concentration, checked *a posteriori* from the Vegard's law of dependence of lattice parameter versus composition ($a_B = 2.8914$ Å) [37], falls in the body-centred cubic A_2 random alloy structure which is stable up to $\sim$ 1773 K. The (110) bulk truncation parameter leads to a rectangular centred surface unit cell the parameters of which are $a_S = 4.0891$ Å and $b_S = 2.8914$ Å along the $[\bar{1}10]_B$ and $[001]_B$ bulk directions, respectively (Fig. 1).

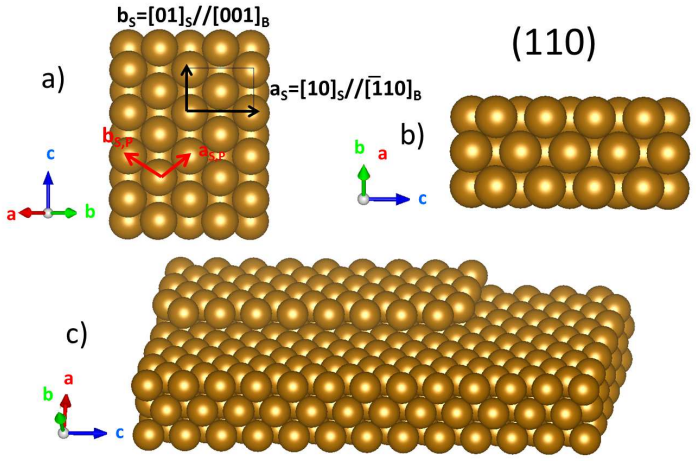

Figure 1: Ball model of the (110) bulk truncation of body-centred cubic $Fe_{0.85}Al_{0.15}$ random alloy. The brown balls stand for the average atom and the bulk cubic unit cell vectors $(\mathbf{a}_B, \mathbf{b}_B, \mathbf{c}_B)$ are shown with coloured arrows. a) Top view along $[110]_B$. The primitive and rectangular unit cells are shown by red and black arrows, respectively. b) Side view along $[1\bar{1}0]_B$. c) View in perspective with a monoatomic step.

After an initial outgassing of the as-received substrate at $T \geq 650$ K, the surface was prepared through cycles of ion sputtering (1 keV, Ar^+) and annealing (duration 20-40 min) in ultra-high vacuum (pressure $< 1.10^{-9}$ mbar) on a dedicated electron bombardment furnace. Temperature (673-1173 K) was determined by an optical pyrometer pointing at the tantalum sample holder and set with an emissivity previously calibrated on a thermocouple

spot-welded on it. The annealing did not exceed 1173 K because of potential Al evaporation problems reported on $Fe_{0.53}Al_{0.47}(110)$ above this temperature [29]. Annealed (110) surfaces were characterized (i) by X-ray Photoelectron Spectroscopy (XPS) on a 5-channeltron hemispherical analyzer (Omicron EA-125) under non-monochromatic Al-Kα excitation (1486.6 eV), (ii) Low Energy Electron Diffraction (LEED) and (iii) Scanning Tunnelling Microscopy (STM). STM was performed in constant current mode at room temperature (Omicron VT SPM) with a tungsten tip electrochemically etched in a KOH solution. Voltage pulses were used to condition the tip on the clean metallic surface. Gwyddion software [38, 39] was used for background subtraction and profile analysis. Due to the very electropositive character of aluminium, contamination from residual background is unavoidable in time during STM measurements. To minimize the effect of ageing in all chemical analysis, photoemission was performed as fast as possible (< 30 min) at a pass energy of $E_P = 20$ eV. If not otherwise specified, photoemission spectra are measured at normal emission. The binding energy scale was calibrated on the Ag $3d_{3/2}$ core level ($E_B = 368.2$ eV). After substraction of a Shirley background [40], core level peak decomposition was performed with Doniach-Sunjic asymmetric profiles [41] for metallic components or gaussian functions for others. A lorentzian broadening of around 0.8 eV due to Al-Kα source was included in peak fitting. Quantification of elements [42, 43, 44] was based on the ratios of peak areas after background subtraction and correction (i) for photo-ionisation cross section of the considered core levels [45] and (ii) for analyser transmission function at the corresponding kinetic energies [46]. This corrected signal is proportional to the atomic concentration and exponentially damped up to the vacuum interface through the so-called inelastic mean free path (IMPF). The integration of the signal depends on the profile of concentration as well on the damping through the crossed layers. Segregation has been modelled in the framework of two schematic approaches, namely a homogeneous mixture and a thin film fully segregated on top of a bulk.

Homogeneous mixture. If an element A is homogeneously mixed with an element B in a bulk $A_{1-x}B_x$, the atomic concentrations are given by $n_A \sim 1 - x$ and $n_B \sim x$. Therefore, the atomic ratio x can be determined from the measured intensities I_A, I_B of given core levels of the elements A and B

from:

$$\frac{I_B}{I_A}\frac{T_A\sigma_A}{T_B\sigma_B} = \frac{x}{1-x}\frac{\lambda_B^{AB}}{\lambda_A^{AB}}, \tag{1}$$

where T_i $(i = A, B)$ is the analyser transmission function at the corresponding electron kinetic energy, σ_i the photo-ionization cross section of the core level under consideration and λ_i^{AB} the inelastic mean free path of the photoelectrons from atom i in $A_{1-x}B_x$.

Thin film on a substrate. For a thin film of thickness t of material B (density n_B) on top of a semi-infinite substrate A (density n_A), the signals are given by:

$$\begin{aligned}
\frac{I_A}{T_A\sigma_A} &\sim n_A \int_{-\infty}^{0} \exp\left(z/\lambda_A^A \cos\Theta\right) dz \times \exp\left(-t/\lambda_A^B \cos\Theta\right) = n_A\lambda_A^A \cos\Theta \exp\left(-t/\lambda_A^B \cos\Theta\right) \\
\frac{I_B}{T_B\sigma_B} &\sim n_B \int_{-t}^{0} \exp\left(z/\lambda_B^B \cos\Theta\right) dz = n_B\lambda_B^B \cos\Theta \left[1 - \exp\left(-t/\lambda_B^B \cos\Theta\right)\right].
\end{aligned} \tag{2}$$

λ_i^j $(i, j = A, B)$ corresponds to the inelastic mean free path of the core level i in the material j and Θ is the emission angle between the analyzer and the substrate normal. Notice that a further damping $\exp\left(-t/\lambda_A^B \cos\Theta\right)$ of the substrate signal in the film has been added in the first equation. The other parameters have the above-defined meanings. The ratio I_B/I_A of intensities yields a transcendental equation that can be solved easily by dichotomy to obtain t from the knowledge of n_A, n_B.

Depending on the material characteristics, the values of inelastic mean free paths were obtained from the TPP-2M predictive formula of Tanuma, Powell and Penn [47, 48, 49, 50, 51, 52, 53, 54, 55] as implemented in the QUASES-IMFP-TPP2M software [56].

3. Results and discussion

Annealing of the sputtered $Fe_{0.85}Al_{0.15}(110)$ led to a transient carbon segregation in the form of self-organized stripes in parallel to a permanent aluminium surface enrichment characterized by a specific superstructure. A thorough photoemission analysis showed the absence of any other common contaminants of iron [57]. After intensive sputtering-annealing cycles, the surface turned out to be carbon free but still aluminium enriched.

3.1. Graphitic films, chemisorbed carbon and carbide

Segregation phenomena were scrutinized through the evolutions of C 1s, Al 2p, Fe 3p core levels and the Auger region of Fe; Fe 3p core level was preferred over the most intense Fe 2p because the proximity in kinetic energy to C 1s and Al 2p minimizes the errors of quantification due to the transmission function of the analyzer. Quantification of the I_{Al2p}/I_{Fe3p} ratio of integrated peak areas for the as-sputtered surface gave a composition $x = 0.19 \pm 0.05$ close to the nominal value $x = 0.15$. Estimates by means of the formula of of Matsumani *et al.* [58] of the sputtering yield of Fe (1.70 atom/ion) and Al (1.53 atom/ion) targets at normal incidence 1 keV Ar^+ ions [59] slightly favour an enrichment of the surface in Al, as observed herein. Noteworthily, the systematic return to the same $I_{Al\,2p}/I_{Fe\,3p}$ value (not shown) demonstrates that sputtering is efficient enough to remove any segregated layer.

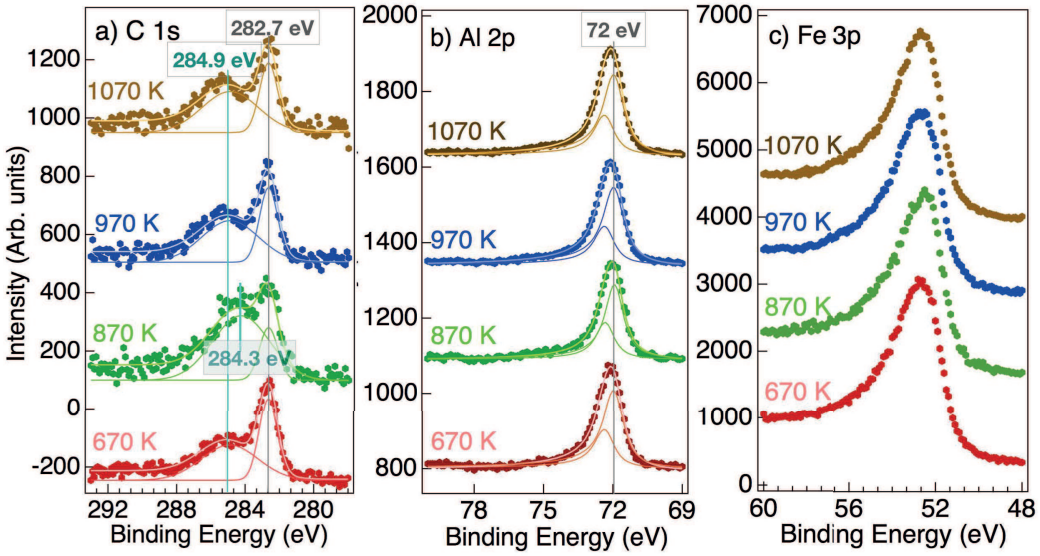

Figure 2: C 1s, Al 2p and Fe 3p core level photoemission spectra recorded upon annealing of the $Fe_{0.85}Al_{0.15}(110)$ surface at 670 K, 870 K, 970 K and 1070 K. XPS spectra are normalised to the maximum intensity of the main peaks. The decomposition of peaks is discussed in the text. Normal emission was used at a pass energy of $E_p = 20$ eV.

Upon annealing between 670 and 1070 K (Fig. 2), besides the presence of C 1s signal, the absence of a shoulder on the high binding energy side of

the metallic Al 2p component at 72 eV (Fig. 2-b) is a clear proof of the bulk origin of the observed carbon. Indeed, studies dedicated to the ageing [35] of carbon-free surfaces have clearly showed that contamination due to residual vacuum (CO and H_2O mainly) is always accompanied by oxidised Al species [35, 60] exhibiting chemical shifts of ~ 2 eV [61], in line with observations made on H_2O and CO adsorption on $Fe_{0.53}Al_{0.47}(110)$ [60]. As shown in Fig. 2-b, the Al 2p peak can be decomposed into only one spin-orbit split (splitting of 0.4 eV [61]) asymmetric Doniach-Sunjic line characteristic of the metallic state [41]. The Al 2p binding energy of 72 eV is shifted by -0.8 eV relative to the pure metal ($E_B = 72.8 \pm 0.3$ eV [61]), as it is found systematically for transition metal aluminides among which $Fe_{0.53}Al_{0.47}$ [60, 62]. A binding energy of 53 eV is observed for Fe 3p in close agreement with literature for the metallic state [61].

At all temperatures but 870 K, the carbon spectra can be decomposed into two components with gaussian shapes, one represented by a rather sharp peak at 282.7 eV with a Full-Width at Half Maximum (FWHM) of 1-1.3 eV and the other by a broad feature at 284.9 eV (3.5-3.9 eV FWHM). These binding energies correspond quite well to those of chemisorbed carbon and graphitic carbon that were found on Fe(100) at 282.6 eV and 284.6 eV [16, 12]. The labelling of the latter [17, 16, 12] comes from the similarities of Auger and photoemission lineshape between graphitic carbon and bulk graphite. Graphene flake on Fe(110) also gives rise to a comparable C 1s binding energy (284.9 eV [13, 63]). Chemisorbed carbon has been associated to a two dimensional surface carbide [12] on Fe(100) which differs from the bulk carbides (Fe_3C or Fe_5C_2) by the C 1s binding energy (283.4 eV to 283.7 eV [16, 64, 65, 66]). In the case of the 870 K annealing, the broad C 1s component peaks at 284.3 eV (Fig. 2) is in agreement with the existence of bulk carbides [67, 16, 18, 64, 65, 66]. However it has not been possible to evidence any change of the Fe 3p line although an upwards shift in binding energy (+0.5 eV [67, 16] between carbide and Fe_3Al; +0.6 eV between carbide and Fe) is expected due to the charge transfer between the two elements [67, 16]. Moreover, the LMV and LVV Auger region of iron involving states in the valence band (Fig. 3) is not affected upon annealing; in particular, no positive peak around 640 eV in kinetic energy is found in the derivative spectra around the $L_3M_{23}V$+Fe 2s transition (Fig. 3-b) while it was shown to be a clear signature of the formation of iron carbide [18]. Although aluminium carbide Al_4C_3 has a C 1s signature at 282.4 eV [68],

its formation can be ruled out since the strong charge transfer to aluminium gives rise to an Al 2p component at 74 eV that is absent in the present measurements. Therefore, the lack of noticeable Fe 3p and Al 2p lineshape evolution upon carbon segregation at 870 K discards the hypothesis of the formation of a significant amount of bulk carbides at that temperature.

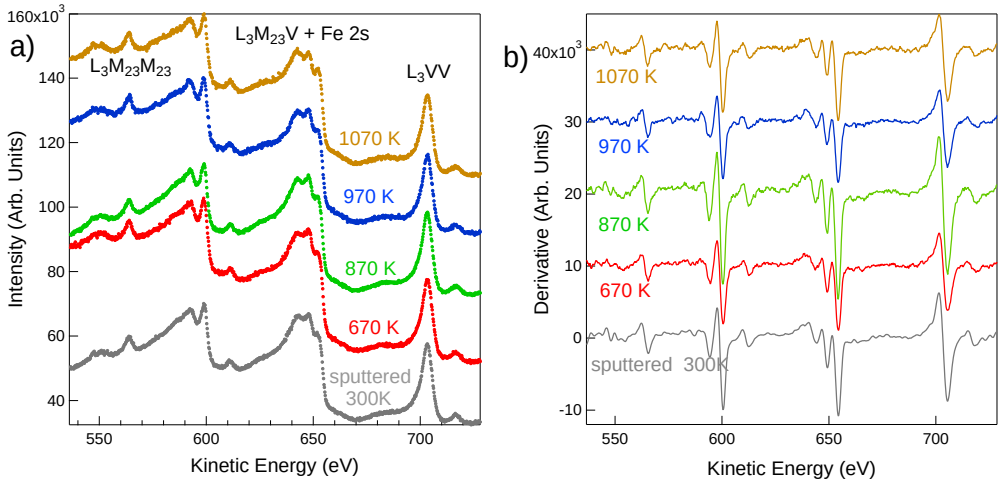

Figure 3: Evolution with temperature of the L_3VV and L_3MV Auger region of iron: a) raw spectra and b) their numerical derivatives. Spectra have been acquired in normal emission at a pass energy of $E_p = 50$ eV; they have been shifted for clarity.

Carbon was quantified as a function of the annealing temperature through the analysis of the ratio of integrated peak areas $I_{C\,1s}/I_{Fe\,3p}$ and $I_{C\,1s}/I_{Al\,2p}$ obtained after profile decomposition and subtraction of a Shirley background (Fig. 4). The two extreme models of homogeneous mixture and fully segregated carbon thin film were compared. Regarding the damping of the photoelectron signal in the hypothetical carbon layer, values of inelastic mean free paths obtained with the TPP-2M formula in bulk graphite (density 2.26 g.cm^{-3}) at Al-Kα excitation were used: $\lambda_{Fe3p}^{graphite} = 38$ Å and $\lambda_{Al2p}^{graphite} = 37.6$ Å. The film thickness was converted in terms of coverage expressed in monolayer as defined by the number of atoms in the (110) surface (1.69×10^{15} atom.cm^{-2}). In a first step, the bulk composition of the alloy required as a reference was assumed to be given by the nominal value $x = 0.15$ (Fig. 4-a,c). The required IMFPs were: $\lambda_{Al2p}^{Fe_{0.85}Al_{0.15}} = 25.4$ Å,

$\lambda_{Fe3p}^{Fe_{0.85}Al_{0.15}} = 25.7$ Å and $\lambda_{C1s}^{Fe_{0.85}Al_{0.15}} = 22.4$ Å. In a second step, the analysis was further refined by taking into account the actual profile of Al segregation (Fig. 4-b,d). This latter was determined through the analysis of the angular dependence of Al 2p/Fe 3p ratio [35, 69] on a carbon free surface obtained after intensive cycles of preparation and annealing above 1100 K in the plateau regime of Al segregation (see Fig .5).

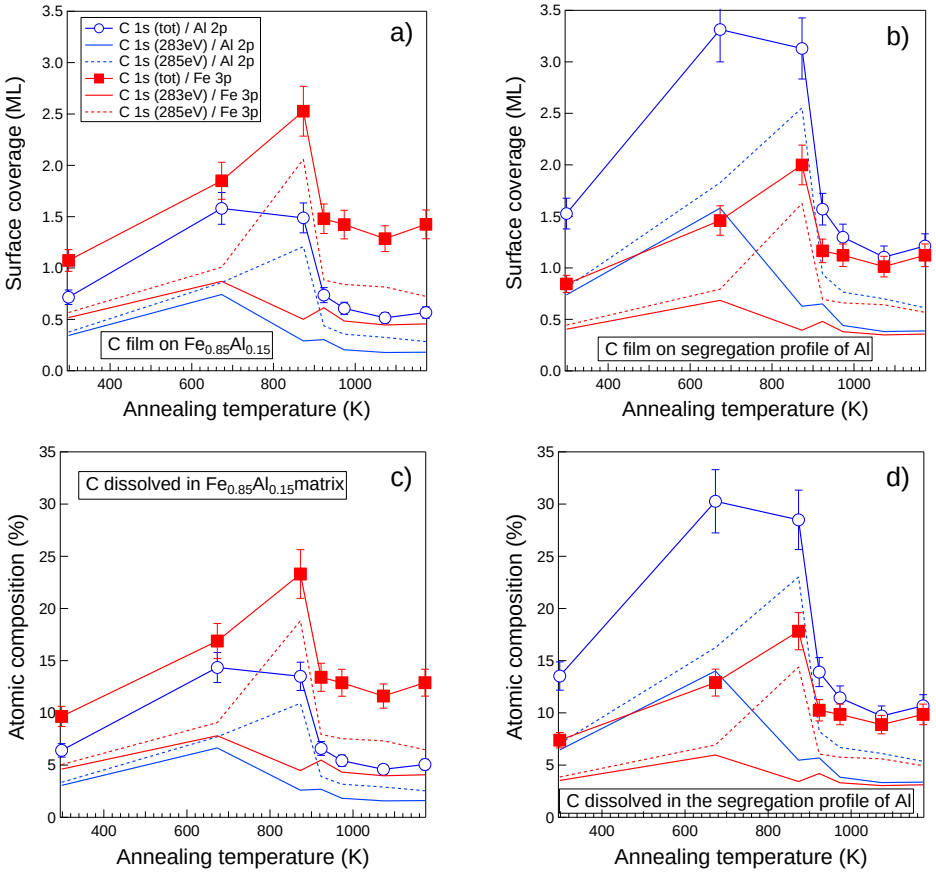

Figure 4: Quantification of carbon coverage from C 1s/Al 2p and C 1s/Fe 3p ratio. a)b) Model of segregated layer and c)d) model of bulk impurities starting from a)c) the $Fe_{0.85}Al_{0.15}$ bulk composition and b)d) the profile of Al segregation (see text). Coverage are given in terms of (110) monolayer. Error bars stem from uncertainties of 10 % on the ratio of intensities.

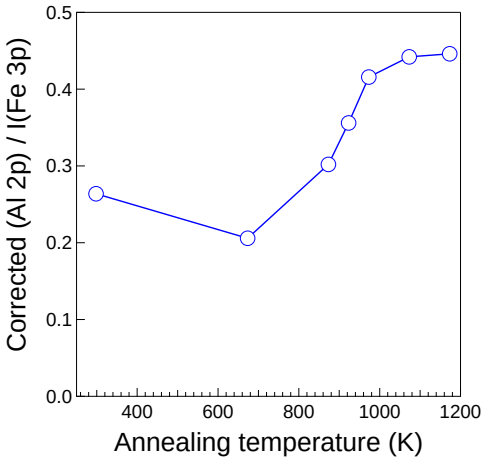

Figure 5: Evolution of the $I_{Al\,2p}/I_{Fe\,3p}$ ratio as function of the annealing temperature on samples showing bulk carbon segregation.

As shown in Fig. 4, the $I_{C\,1s}/I_{Fe\,3p}$ ratio peaks at 870 K prior to a steep decrease. The increase in C 1s intensity is mostly due to the C 1s graphitic component at $>$ 284 eV (Fig. 4). Conversely, the C 1s contribution at 282.7 eV due to chemisorbed carbon is almost constant throughout the annealing process (Fig. 4). The model of carbon homogeneously distributed in the bulk leads to values of carbon concentration (10-25 at.%) which are expected to give rise to a sizeable content of carbides, in particular by annealing at 1070 K. However, nothing in STM (Section 3.2) and photoemission observations can justify such occurrence of carbides. In contrast, the thin carbon film model (Fig. 4-b) in which graphitic carbon dominates up to form 2.5 atomic layers is reminiscent of observations made for similar carbon segregation at the surface of pure iron [15, 16, 70, 21, 20]. The known limit of solubility of carbon in iron (Fig. 6-a) is such that carbon tends to segregate at low temperature to give rise to surface graphite [15, 21, 16, 70], the exact temperature range depending on the carbon content of the metal [15]. At low carbon content, the $Fe_{0.85}Al_{0.15}$ alloy is expected to behave in a way similar to pure iron, which means that it involves the bcc FeAl alloy (instead of bcc iron) and graphite [26]. As for the carbide which is possibly identified at 870 K (Fig. 2-a), it appears in bulk iron at carbon contents higher than the limit of solubility of carbon (Fig. 6-b) [9]. Its formation is endothermic on iron surfaces [65, 10] and it is not favoured on Al-poor bcc FeAl alloys with low carbon content. Therefore, carbide may be observed in the presence of graphitic carbon, but as a minority component [16, 65].

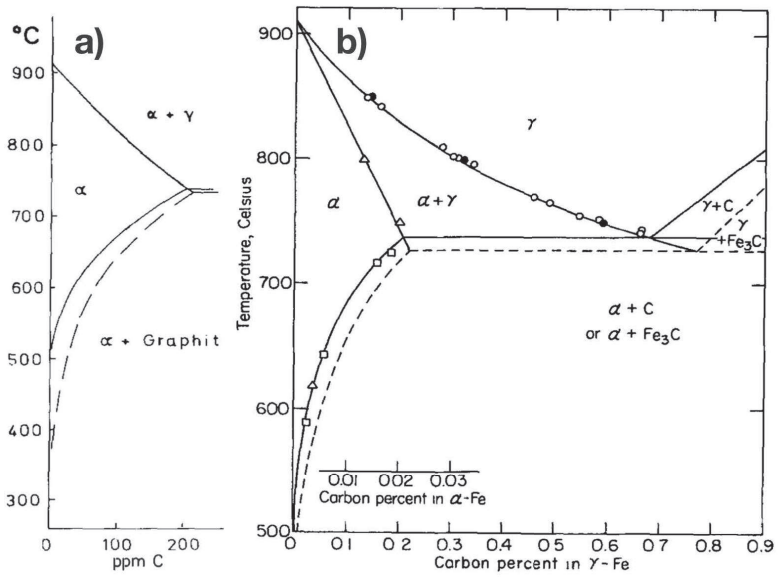

Figure 6: a) Carbon solubility at low-carbon concentration in the α (bcc) phase of the C-Fe binary phase diagram [15]; b) C-Fe phase diagram where the dashed lines indicates the metastable Fe-Fe_3C system. From Ref. [9].

Annealing not only induces carbon segregation but also an enrichment of the surface with aluminium as testified by the increase of $I_{Al\,2p}/I_{Fe\,3p}$ ratio (Fig. 5). Already evidenced on surfaces of ordered FeAl alloys [28, 29, 30, 31, 32, 33, 34] including, to a different extent, the (100), (110) and (111) orientations of $Fe_{0.85}Al_{0.15}$ [35, 69], this phenomenon is driven by the lower surface energy of aluminium compared to iron [71, 72]. The segregation trend leads also to a $FeAl_2$ like surface reconstructions even on Al-rich $Fe_{0.53}Al_{0.47}$(110) surfaces [29, 30]. Therefore, by using as a reference the bulk composition $Fe_{0.85}Al_{0.15}$ (Fig. 4-a,c) for quantification of carbon, a clear discrepancy shows up between results obtained from $I_{C\,1s}/I_{Fe\,3p}$ and $I_{C\,1s}/I_{Al\,2p}$ ratios. However, the profile of segregation found after annealing at high temperature [35] cures the problem (Fig. 4-b,d) above 900 K but worsens it below. As shown in Fig. 5, this onset of temperature corresponds to an enrichment of the surface in Al and to the development of a stationary Al profile of segregation. Conversely, the $Fe_{0.85}Al_{0.15}$ homogeneous alloy model is probably a reliable reference below 600 K where Al segregation is marginal.

3.2. Carbon-induced stripes

3.2.1. STM observation

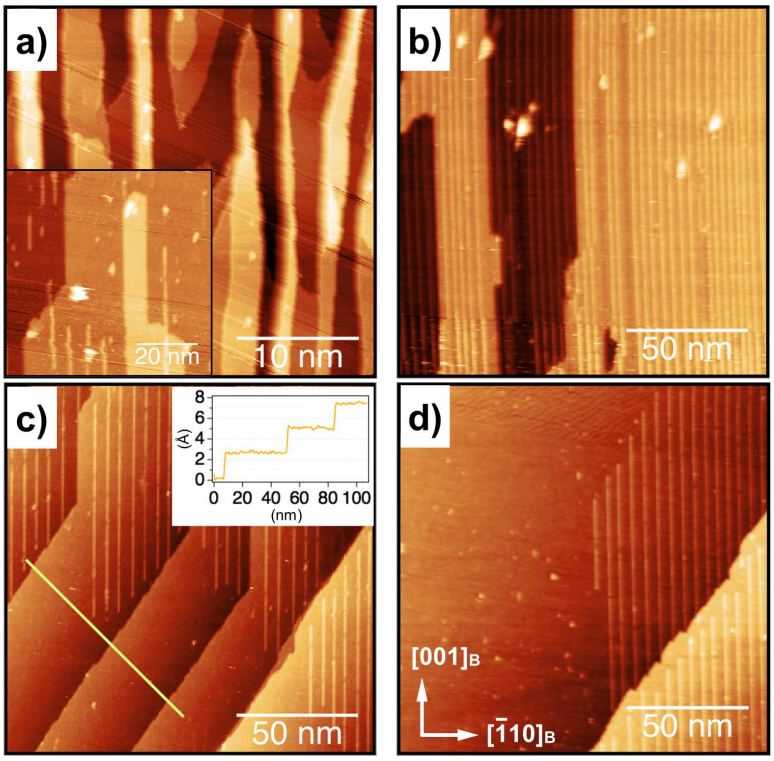

Figure 7: STM imaging of $Fe_{0.85}Al_{0.15}(110)$ upon annealing at increasing temperatures: a) 690 K, 30×30 nm^2, $U_b = -1.0$ V, $I_t = 1.9$ nA; inset: 760 K, 67×67 nm^2, $U_b = +1.7$ V, $I_t = 2$ nA; b) 950 K, 150×150 nm^2, $U_b = -1.0$ V, $I_t = 80$ pA; c) 1030 K, 150×150 nm^2, $U_b = -1.0$ V, $I_t = 80$ pA; inset: height profile corresponding to the line drawn in figure; d) 1070 K, 150×150 nm^2, $U_b = -1.0$ V, $I_t = 1.2$ nA.

As seen in large scale STM images of Fig. 7, the segregation of carbon at the $Fe_{0.85}Al_{0.15}(110)$ surface upon successive annealings parallels the formation of self-organized equidistant stripes of tens to hundreds of nanometres long which protrude over the average surface whatever the bias voltage. This self-organization is likely due to stress effect as in the case of repulsive step-step interactions on metal surfaces [73]. In parallel, a straightening of step edges as well as an enlargement of the terrace size are observed. Below 700 K (Fig. 7-a), the (110) surface shows terraces that are irregular in shape. Be-

tween 690 and 760 K (Fig. 7-a, inset), stripes develop along the $[001]_B$ bulk direction (or $[01]_S$ surface direction) while straight steps form in the same direction. Upon annealing to higher temperatures (Fig. 7-b), the coverage of stripes increases while kinked steps rotated by 142° from $[001]_B$ develop. The step height is found close to 2 Å in agreement with the $a_B/\sqrt{2} = 2.04$ Å bulk $Fe_{0.85}Al_{0.15}$ expectation. Herein, the coverage of stripes is qualitatively determined by calculating the ratio between the apparent area covered by stripes and the corresponding image area. It reaches a maximum of 34 % at 950 K where the average distance between lines is $\sim$ 5 nm, as measured through line profiles along the $[10]_S$ direction (Fig. 8-b inset). When the annealing temperature rises to higher than 1030 K, stripes fade out by decreasing in length leading to a decrease in surface coverage to 13 % and to larger stripe-free domains in which a reconstructed FeAl surface is exposed (Fig. 7-c,d and Fig. 8).

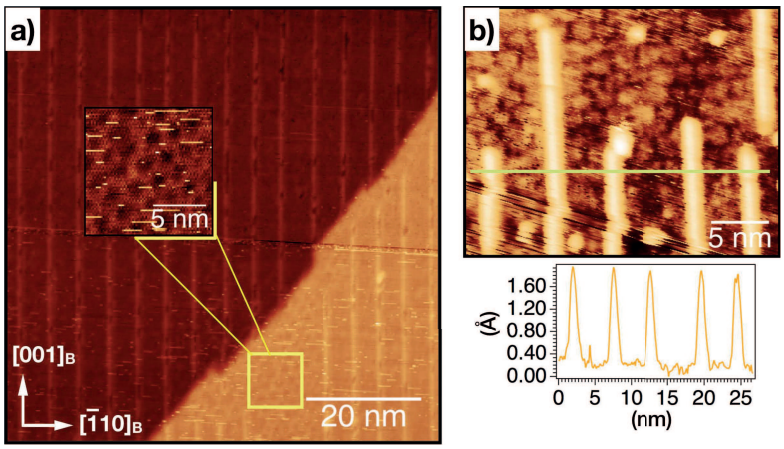

Figure 8: STM images of $Fe_{0.85}Al_{0.15}(110)$ annealed at a) 1030 K, $U_b = -1.0$ V, $I_t = 10$ pA, 75×75 nm^2 and b) 760 K, $U_b = 2$ V, $I_t = 1.97$ nA, 27×21 nm^2. Stripes develop on top of an hexagonal superstructure. The inset corresponds to the line profile shown on the image.

On the enlarged image shown in Fig. 8-a, stripes appear not to be continuous from one terrace to the other. The distance between rows is not constant. It passes through a minimum after annealing at 950 K (Fig. 9-a). Moreover, it shows deviations up to 2 nm. The apparent height of rows varies between 0.5-2.0 Å (Fig. 9-b). It largely depends on the location of

the measurement. Meanwhile, annealing the $Fe_{0.85}Al_{0.15}(110)$ surface also triggers aluminium segregation (Fig. 5 and Ref. [35]). The pseudo-hexagonal superstructure that is observed between stripes (Fig. 8-a) is attributed to the resulting Fe-Al surface compound [35], which will be analysed in detail elsewhere [69]. Differences in contrast that are observed when switching from positive to negative bias (Fig. 8-a,b) are assigned to a chemical contrast in this Al-rich superstructure as observed on transition metal aluminides [74] and on the $FeAl_2$ reconstructions of $Fe_{0.53}Al_{0.47}(110)$ [75].

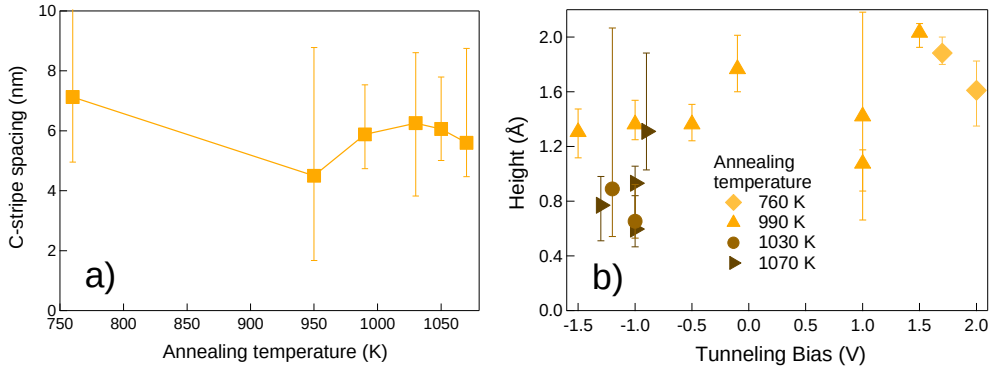

Figure 9: a) Stripe spacing as a function of annealing temperature and b) stripe apparent height as a function of bias voltage derived from a statistical analysis of STM profiles. **Error bars are obtained as the deviation between the maximum/minimum value and the average in a series of measurements.**

The evolution of the stripes coverage as a function of temperature parallels unambiguously that of the intensity of the high-lying C 1s component observed at 284.3-284.9 eV (Fig. 2-a), with a maximum around 900 K (Fig. 4). Such a behaviour indicates that the stripes are associated with graphitic carbon which diffuses partially back into the substrate above 900 K as already observed for dissociatively adsorbed CO on FeAl(110) [60] or segregated carbon on Fe(100) [16, 19]. Carbon desorption is unlikely owing to the low vapor pressure of graphite and to the strong Fe-C bond [15]. In contrast, stripes are not linked to the chemisorbed carbon intensity of which is roughly constant throughout the annealing process. A possible explanation is the competitive segregation of bulk impurities as it was already observed on $Fe_{0.97}Al_{0.03}(100)$ in the order C, Al, S as function of temperature [23]; in

the present case, C 1s signal starts dropping around 900 K (Fig. 4) when the surface enriches in Al (Fig. 5) as on $Fe_{0.97}Al_{0.03}(100)$ [23]. The hierarchy of segregation is likely linked to the related enthalpies that are larger for C ($\Delta H_{Fe(110)} = -117$ kJ/mol [21]) than Al ($\Delta H_{Fe(110)} = -38$ kJ/mol [35]).

3.2.2. LEED discrete diffraction spots

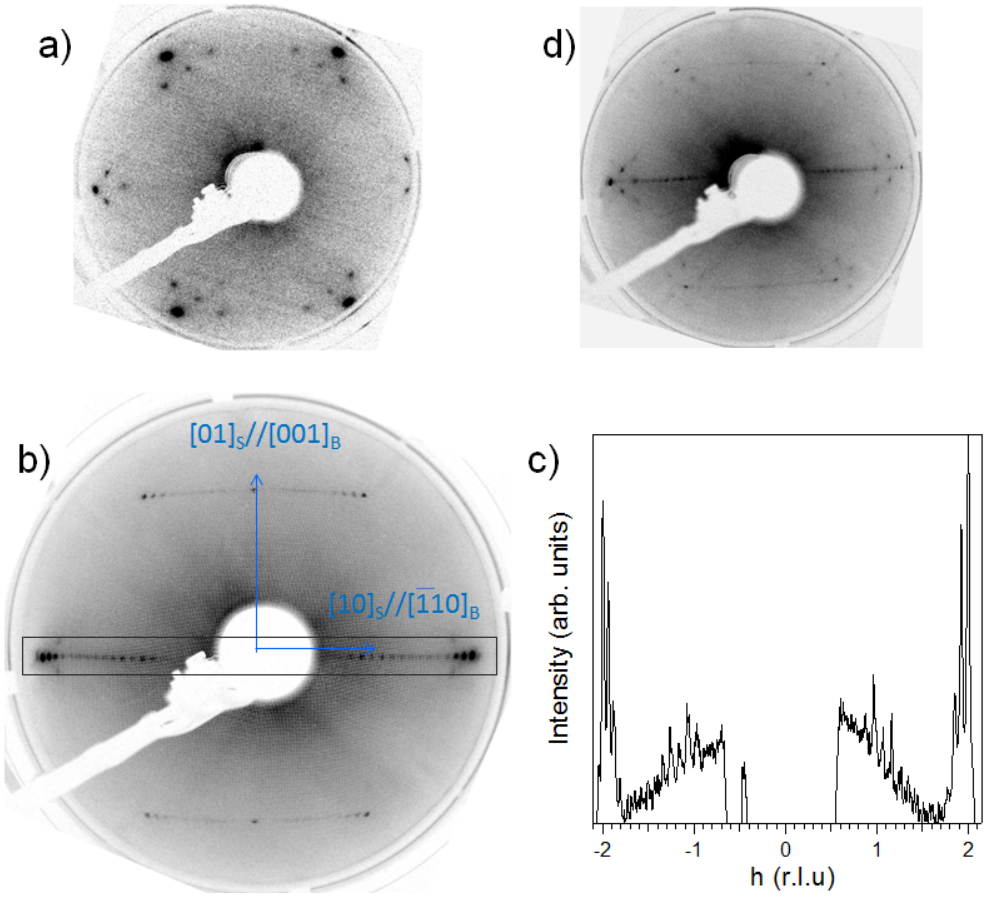

Figure 10: **LEED pattern evolution of a C-containing $Fe_{0.85}Al_{0.15}$(110) surface. a) After annealing at 690 K, the** (1×1) **is overlapped with Al-rich superstructure spots ($E_K = 110$ eV); b) at the maximum of coverage (~ 900 K), spots related to C-stripes are regularly spaced along $[10]_S$ direction ($E_k = 174$ eV) as shown c) by the line cut performed along the indicated box; d) at 1030 K, stripe spots start fading out and lead to a streaking along the $[10]_S$ direction while the superstructure diffraction spots reappear ($E_K = 142$ eV).**

Sputtered (110) surfaces are characterised by a faint (1×1) LEED pattern (not shown) where only the $(11)_S$ spots are present due to the centring of the rectangular surface unit cell. Before carbon stripes apparition, *i.e.* around 690 K, diffraction by a superstructure shows up only around the active $(11)_S$ spots (Fig. 10-a); the crystallographic analysis of this large scale reconstruction will be described elsewhere [35, 69]. The temperature of 690 K corresponds to the onset of segregation of aluminium as shown by photoemission analysis [35] (Fig. 5). Upon further annealing, the "flower"-like patterns sharpen and overlap with discrete spots aligned along the $[10]_S$ direction that give to the pattern a streaked appearance along that direction. These latter sign the occurrence of regularly spaced one-dimensional structures, namely the carbon stripes seen in STM. As already noticed in STM (Fig. 8), Al-rich reconstruction develops not only on C-free terraces but also underneath C-stripes. However, at the maximum of C coverage **around 900 K**, the LEED is clearly dominated by a stripe-related diffraction (Fig. 10-b) in the form of discrete multiple spots with a regular spacing of $\Delta h_S \simeq 0.1$ r.l.u (reciprocal lattice unit) along the $[10]_S$ reciprocal space direction (Fig. 10-c); this corresponds to a periodicity of $a_S/\Delta h_S \simeq 4.3$ nm in good agreement with STM measurements. Finally at 1030 K (Fig. 10-d), the recovering of the "flower"-like spots parallels the disappearance of C-stripes seen in STM and the decay of the graphitic C 1s component. It should be stressed that, besides the mixing of C-stripes and Al-rich reconstruction, the relative contrast of the spots depends strongly on the beam energy. This streaking along the $[10]_S$ of the LEED pattern due to C-segregation resembles to that observed by Graupner *et al.* [29] between 873 and 973 K on the (110) surface of the ordered $Fe_{0.53}Al_{0.47}$ alloy. Although the authors state that their sample was free of contaminants such as carbon, they did not propose any explanation for their observation.

4. Conclusion

The present work investigated in a surface science perspective the poorly explored effect of alloying on carbon segregation at the surface of iron. Carbon impurities in $Fe_{0.85}Al_{0.15}(110)$ single crystal segregate at the surface upon annealing up to 900 K and self-organise in the form of parallel stripes along $[001]_B$ direction. These protruding stripes are several tens to hundreds nanometres long and separated by ~ 5 nm. They are associated to a C 1s

"graphitic" signature that peaks around 900 K like their apparent coverage. At higher temperatures, the surface enriches in aluminium and carbon diffuses back into the bulk, leading to the disappearance of the stripes and to the birth of a hexagonal-like superstructure characteristic of the carbon-free surface. Although stress is likely at the origin of the the self-organization, the mechanism of stripes formation and their actual composition remain unknown and a challenge for theoretical modelling.

5. Acknowledgements

The PhD thesis of Z.D. was funded by the Chinese Scholarship Council and the present work benefited from the support of Agence Nationale de la Recherche in the frame of project SURFOX (ANR-16-CE08-0034-01).

[1] http://www.worldautosteel.org/.

[2] S. Deevi, V. Sikka, Nickel and iron aluminides: An overview on properties, processing, and applications, Intermetallics 4 (5) (1996) 357–375.

[3] H. J. Grabke, Surface and grain boundary segregation on and in iron and steels, ISIJ International 29 (7) (1989) 529–538.

[4] R. Cavallotti, Effets de la terminaison de l'α-alumine sur le comportement au mouillage du zinc, Ph.D. thesis, Université Pierre et Marie Curie, France (2014).

[5] R. Cavallotti, J. Goniakowski, R. Lazzari, J. Jupille, A. Koltsov, D. Loison, Role of surface hydroxyl groups on zinc adsorption characteristics on $\alpha-Al_2O_3(0001)$ surfaces: first-principles study, J. Phys. Chem. C 118 (2014) 13578–13589.

[6] R. Cavallotti, H.-L. Thi Le, J. Goniakowski, R. Lazzari, J. Jupille, A. Koltsov, D. Loison, New routes for engineering the adhesion at $Zn/\alpha-Al_2O_3(0001)$ interface, Phys. Chem. Chem. Phys. 18 (2016) 3032–3039.

[7] H.-A. T. Le, J. Goniakowski, C. Noguera, A. Koltsov, J.-M. Mataigne, First-principles study on the effect of pure and oxidized transition-metal buffers on adhesion at the alumina/zinc interface, J. Phys. Chem. C 120 (2016) 9836–9844.

[8] H.-L. Thi Le, R. Lazzari, J. Goniakowski, S. Cavallotti, R. Chenot, C. Noguera, J. Jupille, A. Koltsov, J.-M. Mataigne, Tuning adhesion at metal/oxide interfaces by surface hydroxylation, J. Phys. Chem. C 121 (2017) 11464–11471.

[9] J. Chipman, Thermodynamics and phase diagram of the Fe-C system, Metall. Trans. 3 (1) (1972) 55–64.

[10] D. Jiang, E. Carter, Carbon atom adsorption on and diffusion into Fe(110) and Fe(100) from first principles, Phys. Rev. B 71 (4) (2005) 045402.

[11] X. W. Liu, C. F. Huo, Y. W. Li, J. Wang, H. Jiao, Energetics of carbon deposition on Fe(100) and Fe(110) surfaces and subsurfaces, Surf. Sci. 606 (2012) 733 – 739.

[12] C. Uebing, Two-dimensional transition metal compounds with carbon, nitrogen and oxygen on bcc(100) metal and alloy surfaces, Prog. Solid State Chem. 26 (1998) 155 – 240.

[13] N. A. Vinogradov, A. A. Zakharov, V. Kocevski, J. Rusz, K. A. Simonov, O. Eriksson, A. Mikkelsen, E. Lundgren, A. S. Vinogradov, N. Mårtensson, A. B. Preobrajenski, Formation and structure of graphene waves on Fe(110), Phys. Rev. Lett. 109 (2012) 026101.

[14] H. J. Grabke, G. Tauber, H. Viefhaus, Equilibrium surface segregation of carbon on iron (100) faces, Scr. Metall. 9 (1975) 1181 – 1184.

[15] H. Grabke, W. Paulitschke, G. Tauber, H. Viefhaus, Equilibrium surface segregation of dissolved nonmetal atoms on iron (100) faces, Surf. Sci. 63 (1977) 377–389.

[16] G. Panzner, W. Diekmann, The bonding state of carbon segregated to α-iron surfaces and on iron carbide surfaces studied by electron spectroscopy, Surf. Sci. 160 (1) (1985) 253–270.

[17] H. Bonzel, H. Krebs, On the chemical nature of the carbonaceous deposits on iron after CO hydrogenation, Surf. Sci. 91 (1980) 499 – 513.

[18] C. S. Kuivila, J. B. Butt, P. C. Stair, Characterization of surface species on iron synthesis catalysts by X-ray photoelectron spectroscopy, Appl. Surf. Sci. 32 (1988) 99–121.

[19] A. Wiltner, C. Linsmeier, T. Jacob, Carbon reaction and diffusion on Ni(111), Ni(100), and Fe(110): Kinetic parameters from x-ray photoelectron spectroscopy and density functional theory analysis, J. Chem. Phys. 129 (2008) 084704.

[20] G. Panaccione, J. Fujii, I. Vobornik, G. Trimarchi, N. Binggeli, A. Goldoni, R. Larciprete, G. Rossi, Local and long-range order of carbon impurities on Fe(100): Analysis of self-organization at a nanometer scale, Phys. Rev. B 73 (3) (2006) 035431.

[21] S. Kelemen, A. Kaldor, The interaction of surface sulfur with carbon on Fe(110), J. Chem. Phys. 75 (3) (1981) 1530–1537.

[22] P. Dumoulin, M. Guttmann, The influence of chemical interactions between metallic and metalloid solutes on their segregation in $\alpha-$Fe I: Co-segregation at free surface studied by Auger electron spectroscopy, Mat. Sci. and Eng. 42 (1980) 249 – 263.

[23] V. Blum, A. Schmidt, W. Meier, L. Hammer, K. Heinz, Competitive surface segregation of C, Al and S impurities in Fe(100), J. Phys.: Condens. Matter 15 (2003) 3517–3529.

[24] B. W. Busch, C. Uebing, T. Gustafsson, Rocksalt CrC formation on the Fe-15%Cr(100) surface, Phys Rev B 64 (2001) 115427.

[25] O. Kubaschewski, Iron binary phase diagrams, Springer Science & Business Media, 2013.

[26] M. Palm, G. Inden, Experimental determination of phase equilibria in the Fe-Al-C system, Intermetallics 3 (1995) 443–454.

[27] R. Besson, A. Legris, D. Connetable, P. Maugis, Atomic-scale study of low-temperature equilibria in iron-rich Al-C-Fe, Phys. Rev. B 78 (2008) 014204.

[28] M. Gemmaz, M. Afyouni, A. Mosser, Determination of the diffusion coefficient of Al in Fe-Al alloy by Auger spectrometry, Surf. Sci. Lett. 227 (1990) L109–L11.

[29] H. Graupner, L. Hammer, K. Müller, D. Zehner, Composition and structure of the (100) and (110) surfaces of FeAl, Surf. Sci. 322 (1995) 103–115.

[30] L. Hammer, H. Graupner, V. Blum, K. Heinz, G. Ownby, D. Zehner, Segregation phenomena on surfaces of the ordered bimetallic alloy FeAl, Surf. Sci. 412-413 (1998) 69–81.

[31] K. Heinz, L. Hammer, Surface structure and segregation of bimetallic bcc-type alloys, J. Phys.: Condens. Matter 11 (43) (1999) 8377.

[32] V. Blum, L. Hammer, W. Meier, K. Heinz, M. Schmid, E. Lundgren, P. Varga, Segregation and ordering at $Fe_{1-x}Al_x$ (100) surfaces : a model case for binary alloys, Surf. Sci. 474 (1) (2001) 81–97.

[33] W. Meier, V. Blum, L. Hammer, K. Heinz, Equilibration of stoichiometrically distorted $Fe_{1-x}Al_x$ (100) surfaces, J. Phys.: Condens. Matter 13 (9) (2001) 1781–1791.

[34] L. Hammer, W. Meier, V. Blum, K. Heinz, Equilibration processes in surfaces of the binary alloy Fe-Al, J. Phys: Condens. Matter 14 (2002) 4145–4164.

[35] Z. Dai, Orientation-dependent segregation and oxidation at $Fe_{0.85}Al_{0.15}$ random alloy surfaces, Ph.D. thesis, University Pierre et Marie Curie, France (2017).

[36] http://www.physik.de/mateck.

[37] M. Ellner, I. Park, On the partial atomic volume of aluminum in solid solutions based on the 3d transition metals and copper, Metallurgical and Materials Transactions A 33 (2002) 3591–3595.

[38] Gwyddion software, http://gwyddion.net/.

[39] D. Necas, P. Klapetek, Gwyddion: an open-source software for SPM data analysis, Cent. Eur. J. Phys. 10 (2012) 181–188.

[40] D. Shirley, High-resolution X-ray photoemission spectrum of valence bands of gold, Phys. Rev. B 5 (1972) 4709–4714.

[41] S. Doniach, M. Sunjic, Many-electron singularity in x-ray photoemission and x-ray line spectra from metals, Journal of Physics Part C : Solid State Physics 3 (1970) 285–291.

[42] S. Hofmann, Auger and X-ray photoelectron spectroscopy in material science, Springer, 2013.

[43] J. F. Moulder, W. F. Stickle, P. E. Sobol, K. D. Bomben, Handbook of X-ray photoelectron spectroscopy, Physical Electronics, Inc., 1995.

[44] C. D. Wagner, W. M. Riggs, L. E. Davis, J. F. Moulder, G. E. Muilenberg, Handbook of X-Ray Photoelectron spectroscopy, Perkin-Elmer, Eden Prairie, 1979.

[45] J. Yeh, I. Lindau, Atomic subshell photoionization cross sections and assymetry parameters: $1 \leq z \leq 300$, At. Data Nucl. Data Tables 32 (1985) 1–155.

[46] P. Ruffieux, P. Schwaller, O. Gröning, L. Schlapbach, P. Gröning, Q. C. Herd, D. Funnemann, J. Westermann, Experimental determination of the transmission factor for the Omicron EA125 electron analyzer, Rev. Sci. Instr. 71 (2000) 3634–3639.

[47] S. Tanuma, C. J. Powell, D. R. Penn, Calculations of electron inelastic mean free paths for 31 materials, Surf. Interface Anal. 11 (11) (1988) 577–589.

[48] S. Tanuma, C. J. Powell, D. R. Penn, Calculations of electron inelastic mean free paths: II Data for 27 elements over the 50-2000 eV range, Surf. Interface Anal. 17 (1991) 911–926.

[49] S. Tanuma, C. J. Powell, D. R. Penn, Calculations of electron inelastic mean free paths: III Data for 15 inorganic compounds over the 50-2000 eV range, Surf. Interface Anal. 17 (1991) 927–939.

[50] S. Tanuma, C. J. Powell, D. R. Penn, Calculations of electron inelastic mean free paths (IMFPS). IV. Evaluation of calculated IMFPs and of the predictive IMFP formula TPP-2 for electron energies between 50 and 2000 eV, Surf. Interface Anal. 20 (1) (1993) 77–89.

[51] S. Tanuma, C. J. Powell, D. R. Penn, Calculations of electron inelastic mean free paths. V. Data for 14 organic compounds over the 50-2000 eV range, Surf. Interf. Anal. 21 (1994) 165–176.

[52] S. Tanuma, C. J. Powell, D. R. Penn, Calculations of electron inelastic mean free paths (IMFPs) VI. analysis of the Gries inelastic scattering model and predictive IMFP equation, Surf. Interface Anal. 25 (1) (1997) 25–35.

[53] S. Tanuma, C. J. Powell, D. R. Penn, Calculation of electron inelastic mean free paths (IMFPs) VII. reliability of the TPP-2M IMFP predictive equation, Surf. Interface Anal. 35 (3) (2003) 268–275.

[54] S. Tanuma, C. J. Powell, D. R. Penn, Calculations of electron inelastic mean free paths, Surf. Interface Anal. 37 (1) (2005) 1–14.

[55] H. Shinotsuka, S. Tanuma, C. J. Powell, D. R. Penn, Calculations of electron inelastic mean free paths. X. Data for 41 elemental solids over the 50 eV to 200 keV range with the relativistic full Penn algorithm, Surf. Interface Anal. 47 (9) (2015) 871–888.

[56] S. Tougaard, QUASES-IMFP-TPP2M Software, http://www.quases.com/products/quases-imfp-tpp2m/.

[57] R. Musket, W. McLean, C. Colmenares, D. Makowiecki, W. Siekhaus, Preparation of atomically clean surfaces of selected elements: A review, Applications of Surface Science 10 (2) (1982) 143 – 207.

[58] N. Matsunami, Y. Yamamura, Y. Itikawa, N. Itoh, Y. Kazumata, S. Miyagawa, K. Morita, R. Shimizu, H. Tawara, Energy dependence of the ion-induced sputtering yields of monatomic solids, At. Data Nucl. Data Tables 31 (1984) 1–80.

[59] A simple sputter yield calculator, https://www.iap.tuwien.ac.at/www/surface/sputteryield.

[60] N. Gleason, D. Strongin, A photoelectron spectroscopy and thermal desorption study of CO on FeAl (110) and polycrystalline TiAl and NiAl, Surf. Sci. 295 (3) (1993) 306–318.

[61] NIST X-ray photoelectron spectroscopy database, https://srdata.nist.gov/xps/Default.aspx.

[62] H. Graupner, L. Hammer, K. Heinz, D. Zehner, Oxidation of low-index FeAl surfaces, Surf. Sci. 380 (1997) 335.

[63] N. A. Vinogradov, K. A. Simonov, A. V. Generalov, J. Drnec, F. Carlà, A. S. Vinogradov, A. B. Preobrajenski, N. Mårtensson, R. Felici, The structural evolution of graphene/Fe(110) systems upon annealing, Carbon 111 (2017) 113 – 120.

[64] W. Arabczyk, F. Storbeck, H. Müssig, Electron spectroscopy studies on carbon segregation from a mono-crystalline α-Fe (111) specimen, Appl. Surf. Sci. 65 (1993) 94–98.

[65] A. Wiltner, C. Linsmeier, Formation of endothermic carbides on iron and nickel, Phys. Status Solidi A 201 (5) (2004) 881–887.

[66] E. Papastavros, P. Shea, M. Langell, Oxygen, carbon, and sulfur segregation in annealed and unannealed zerovalent iron substrates, Langmuir 20 (26) (2004) 11509–11516.

[67] I. N. Shabanova, V. A. Trapeznikov, A study of the electronic structure of Fe_3C, Fe_3Al and Fe_3Si by x-ray photoelectron spectroscopy, J. Electron Spectrosc. Relat. Phenom. 6 (1975) 297 – 307.

[68] C. Hinnen, D. Imbert, J. M. Siffre, P. Marcus, An *in situ* XPS study of sputter-deposited aluminium thin films on graphite, Appl. Surf. Sci. 78 (1994) 219 – 231.

[69] To be published.

[70] J. Fujii, G. Panaccione, I. Vobornik, G. Rossi, G. Trimarchi, N. Binggeli, C-Fe chains due to segregated carbon impurities on Fe(100), Surf. Sci. 600 (2006) 3884–3887.

[71] W. Tyson, W. Miller, Surface free energies of solid metals: Estimation from liquid surface tension measurements, Surf. Sci. 62 (1977) 267.

[72] L. Vitos, A. Ruban, H. Skriver, J. Kollár, The surface energy of metals, Surf. Sci. 411 (1998) 186.

[73] P. Muller, Elastic effects on surface physics, Surf. Sci. Rep. 54 (5-8) (2004) 157–258.

[74] T. Duguet, P. A. Thiel, Chemical contrast in STM imaging of transition metal aluminides, Prog. Surf. Sci. 87 (2012) 47 – 62.

[75] O. Kizilkaya, D. Hite, D. Zehner, P. Sprunger, Surface reconstruction of FeAl(110) studied by scanning tunnelling microscopy and angle-resolved photoemission spectroscopy, J. Phys.: Condens. Matter 16 (30) (2004) 5395–5406.